ORIGINAL ARTICLE

AtmoFlow - Investigation of Atmospheric-Like Fluid Flows Under Microgravity Conditions

F. Zaussinger[1] · P. Canfield[2] · A. Froitzheim[1] · V. Travnikov[1] · P. Haun[1] · M. Meier[1] · A. Meyer[1] · P. Heintzmann[3] ·
T. Driebe[3] · Ch. Egbers[1]

Abstract

The main objective of the *AtmoFlow* experiment is the investigation of convective flows in the spherical gap geometry. Gaining fundamental knowledge on the origin and behavior of flow phenomena such as global cells and planetary waves is interesting not only from a meteorological perspective. Understanding the interaction between atmospheric circulation and a planet's climate, be it Earth, Mars, Jupiter, or a distant exoplanet, contributes to various fields of research such as astrophysics, geophysics, fluid physics, and climatology. AtmoFlow aims to observe flows in a thin spherical gap that are subjected to a central force-field. The Earth's own gravitational field interferes with a simulated central force-field with the given parameters of the model which makes microgravity conditions of $g < 10^{-3}\,g_0$ (e.g. on the ISS) necessary. Without losing its overall view on the complex physics, circulation in planetary atmospheres can be reduced to a simple model of a central gravitational field, the incoming and outgoing energy (e.g. radiation) and rotational effects. This strongly simplified assumption makes it possible to break some generic cases down to test models which can be investigated by laboratory experiments and numerical simulations. Varying rotational rates and temperature boundary conditions represent different types of planets. This is a very basic approach, but various open questions regarding local pattern formation or global planetary cells can be investigated with that setup. A concept has been defined for developing a payload that could be installed and utilized on-board the International Space Station (ISS). This concept is based on the microgravity experiment *GeoFlow*, which has been conducted successfully between 2008 and 2016 on the ISS. This paper addresses the scientific goals, the experimental setup, the concept for implementation of the AtmoFlow experiment on the ISS and first numerical results.

Keywords Microgravity conditions · Rotating convection · Atmospheric flows · Dielectrophoresis · Dielectric heating

Introduction

In a first approximation planetary atmospheres are confined fluid layers between two spherical shells. Hence, the fluid flow is determined by the boundaries of the system, which are the inner and outer shell. The inner shell represents the planetary surface or deep, blocking atmospheric layers of e.g. gas giants. The outer shell represents the upper boundary of the climate-relevant atmosphere or, in case of the gas giant, a region, where the gas concentration decreases significantly. This simplified setup makes it possible to break some generic cases to test models, which can be investigated in laboratory experiments and numerical simulations. The main advantage of such an experiment is the reproducibility and the ability to resolve scales, which are parameterized by semi-empirical closure models, see e.g. Scolan and Read (2017).

However, such laboratory experiments are difficult to establish. Earth's gravity field would dominate or at least significantly contribute to any radial force field of a spherical experiment, which makes it very difficult to deduce meaningful results because of the relative

✉ F. Zaussinger
    florian.zaussinger@b-tu.de

[1] Department of Aerodynamics and Fluid Mechanics, Brandenburg University of Technology Cottbus-Senftenberg, Cottbus, Germany

[2] Airbus Defence and Space GmbH, Immenstaad, Germany

[3] Deutsches Zentrum für Luft- und Raumfahrt e.V., Bonn, Germany

magnitude. The centrifugal force can be used as radial force field to mimic buoyancy. However, this works only for the fast rotating case, see e.g. Busse and Carrigan (1976), and needs an inverted thermal gradient (outer shell heated, inner shell cooled) to establish a convectively unstable system. This setup cannot be used to investigate non-rotating cases and fluid flows with complex boundary conditions. The projection of a hemisphere onto a cylinder is one way to overcome some of the the problems e.g. to make use of a baroclinic wave tank (Borcia and Harlander 2013; Vincze et al. 2015), though various phenomena such as equatorial waves cannot be investigated with this setup. The most promising solution is to set up a spherical gap experiment with a radial force field in a microgravity environment. By applying laterally varying temperature boundary conditions and differential rotation it is possible to simulate a deep planetary atmosphere, where features like planetary waves and complex pattern formation can be studied. Indeed, the main advantage of the experiment proposed in this paper is the full sphere setup, which allows investigating equatorial zonal flows and also allows to distinguish equatorially symmetric and antisymmetric contributions.

Various experiments under microgravity conditions have been performed in the scope of fluid dynamics and convection. The half-dome experiment by Hart et al. (1986) on SpaceLab mission in 1986 was the first microgravity experiment utilizing the dielectrophoretic effect (DEP). Hart's experiment used lateral heating sources, corresponding to planetary atmosphere boundary conditions. Additionally, the experiment was mounted on a rotating table. They investigated columnar cells and their interaction with mid-latitude waves. Even spiral waves and non-axisymmetric convection zones were observed.

Channel flow experiment were conducted by Smirnov et al. (2004), where a Hele-Shaw cell was exposed to microgravity conditions on parabolic flight campaigns. They investigated the displacement of viscous fluid and showed that the increase of the viscosity ratio between two miscible fluids increases the fingering instability. Flow rate limitations in single phase and two phase open capillary channel flows were examined in an experiment setup on the ISS in addition to examining the effect of the geometry of the channel on the stability of the free surface (Canfield et al. 2013; Conrath et al. 2013). The investigators also focused on bubble formation (Canfield 2018), surface-tension driven bubble migration, and passive phase separation (Jenson et al. 2014). The mission lasted multiple months and yielded video material for thousands of data points within a wide range of parameters (Bronowicki et al. 2015).

The first german experiment investigating convective flows in microgravity conditions was conducted on a parabolic flight campaign in 1991, Liu et al. (1992). In the following, similar experiments had been performed on the

TCM Volna ballistic rocket, see e.g. Egbers et al. (1999), Kuhl et al. (2005). During the flight of this rocket the experiment was able to be conducted for about 20 min under microgravity conditions. Based on this first experiment the spherical gap experiment GeoFlow (geophysical flow) was developed in the early 2000s and successfully run on the ISS between 2008 and 2016, (Egbers et al. 2003; Beltrame et al. 2003; Travnikov et al. 2003; Ezquerro Navarro et al. 2015). The GeoFlow experiment was designed to study convective flows whilst applying a radial temperature gradient. Two missions were successfully completed in the scope of this experiment, GeoFlow I (GFI) and GeoFlow II (GFII).

Both experiments have been conducted on the ISS within the Fluid Science Laboratory (FSL) of the Columbus module, but, with differing working fluids. The main advantage of GeoFlow is its full sphere geometry, where basic features of iso-viscous convection (GFI: Futterer et al. (2008); Jehring et al. (2009)) and flows with temperature-dependent viscosity (GFII: Futterer et al. (2013); Zaussinger et al. (2017, 2018b); Travnikov et al. (2017)) have been studied.

Besides the GeoFlow experiments, an experimental setup dedicated to parabolic flight campaigns (PFC) has been developed, too, see Futterer et al. (2016) and Meier et al. (2018). Based on the same physical mechanism, thermo-electric convection is studied inside a cylindrical annulus (Meyer et al. 2017, 2018). Between 2016 and 2018, four campaigns successfully displayed the occurrence of convective instability caused by DEP-force during low gravity phases (22 sec of 10^{-2} g$_0$) with different fluids, aspect ratios and control parameters.

While thermo-electric convection in a cylindrical gap is a simplified model for the GeoFlow and AtmoFlow spherical geometries, it has also direct applications such as cylindrical heat exchangers for electronic devices, see e.g. Evgenidis et al. (2011), Lotto et al. (2017).

The proposed experiment AtmoFlow differs much from the previous GeoFlow-setups. First, the inner and the outer boundaries will both be heated/cooled locally. Additionally, a differential rotating unit is foreseen, to simulate deep shells, as they occur in giant planets. Figure 1 depicts such a simplified atmosphere, where incoming radiation and rotation lead to global cell formation. These cells (Hadley cell, Ferrel cell or mid-latitude cell, polar cell) are well known from the Earth and co-responsible for global atmospheric dynamics. In contrast to Hart's experiment, AtmoFlow is designed as a (nearly) full sphere. The advantage of this design is apparent, when equatorial flows and global patterns are investigated. AtmoFlow will be the first experiment under microgravity conditions, which will be able to study simplified global fluid flows, planetary waves and complex patterns in the full spherical shell geometry under atmospheric-like boundary conditions.
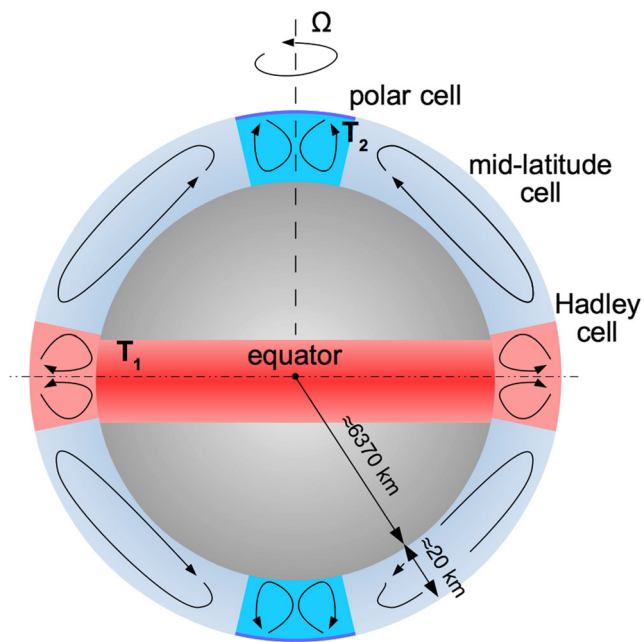
Fig. 1 Simplified planetary atmosphere as found on the Earth. Not to scale.

The empirical study of planetary waves, global cell formation and fluid dynamical instabilities are in the focus of the experiment. The experiment results will provide benchmark data for a rich variety of numerical problems, which are still a challenge for scientific research in various fields.

This paper is structured as follows. Section "Objectives and Scientific Program" gives an overview of the objectives and the scientific program of the AtmoFlow experiment. A brief description of the experiment is presented in Section "Brief Description of the Experiment". The experimental methods and diagnostics are presented in Section "Experimental Methods and Diagnostics". This includes a g_0 testing facility on ground, where $g_0 = 9.81$ m/s^2. The physics of thermo-electro hydrodynamics and the dielectrophoretic effect are described in Section "Thermo-Electro Hydrodynamics". Results from accompanying numerical simulations are presented in Section "Numerical Simulations". We summarize the content of our findings in Section "Conclusions and Outlook".

Objectives and Scientific Program

The AtmoFlow experiment makes it possible to investigate flows, which are driven by internal heating, boundary temperature difference, rotation or complex boundary conditions. It will enable deep insights into EHD driven fluid flows, which can be used for validating simple convection

models of planetary atmospheres. The extension of semi-empirical parameterizations of unresolved atmospheric processes, e.g. large-scale / small-scale coupling will be investigated, too. Furthermore, precise parametrization of cell formation will be tested with respect of e.g. Rhines scaling, Read et al. (2004); Heimpel et al. (2005). This includes the investigation of the heat transfer from the tropics to the stably stratified mid-latitudes, Scolan and Read (2017). In addition, the findings of AtmoFlow are expected to be of benefit for validation and development of models that deal with climate change. Various initial temperature distributions will be tested to investigate connections between external forcing and climate variability.

The main goal is the elucidation of basic aspects of convection in the rotating spherical shell. This allows the testing of linear stability analysis regarding base flows, convective onsets and bifurcation scenarios in rotating and non-rotating scenarios. Planned applications are presented subsequently:

Non-Rotating Case

The *non-rotating case* is mainly used to test physical models of electro-hydrodynamics. Especially, the role of mixed heating (internal heating and temperature difference across the gap) is not well understood in the spherical gap geometry, see .e.g. Vilella and Deschamps (2018). Even though the non-rotating case has no direct geo- or astrophysical counterpart, it is of importance for planned technical applications. The construction of optimized heat exchangers, EHD-based pumps and nozzles will profit from this research. Furthermore, the enhancement of convective heat transfer in absence of gravity (e.g. on space stations or spacecrafts) will benefit from from a deeper understanding of EHD driven fluid flows.

Rotating Case

AtmoFlow captures only a small range of realistic geo- and astrophysical parameters. Here, we refer to Section "Thermo-Electro Hydrodynamics" where all dimensionless numbers are defined. The size and weight of the payload limits the Rayleigh number to Ra $< 10^6$, the Taylor number to Ta $< 10^7$, the Ekman number to $10^{-2} <$ Ek $< 10^{-3}$, the Prandtl number to Pr $= 8$ and the Rossby number to $|$Ro$| < 4$. However, many rotating flows can be studied with this setup. In the following, typical applications, limitations and the parameter regimes for proposed research scenarios of rotating AtmoFlow experiments are presented:

– *Convection*, more precisely the convective onset, transitions to the turbulent regime and symmetry-breaking bifurcations (Mamun and Tuckerman 1995;

Feudel et al. 2015) are compared with linear stability analysis and numerical simulations in the super-critical range of Ra/Ra$_{crit}$ < 20 and the entire given Taylor number regime. These experiments will be conducted either with internal heating and/or a temperature difference across the gap.

– *Torsional oscillations* and resulting radial equatorial jets (Vorontsov et al. 2002; Hollerbach et al. 2002) can be investigated in the entire parameter range for Re > 100. Such experiments depend only on inner sphere dynamics and not on the thermal distribution.

– Several questions arise in the scope of *zonal wind systems* like those found on Jupiter or Saturn. AtmoFlow represents a deep-seated experiment with geometric properties and Ekman numbers comparable to early 3d-simulations by e.g. Christensen (2001) and laboratory experiments e.g. Manneville and Olson (1996). The direction of the jets (super-rotation and retrograde equatorial flows) are found to correlate with the convective Rossby number $Ro_T = \sqrt{Ra/Pr}\,Ek$. According to definitions by Julien et al. (2012) and Gastine et al. (2013a), the AtmoFlow experiment ranges between $10^{-1} < Ro_T < 10$. The lower limits of Ro_T cover roughly flow regimes as found on planets of our solar system (Wang and Read 2012) e.g. $Ro_T = 0.5$ on Jupiter's surface, (Gastine et al. 2013a). Hence, the basic investigation of zonal winds and the role of Ro_T regarding super-rotation as found on Jupiter or Saturn (Gastine et al. 2013b) as well as retrograde equatorial jets known from Uranus and Neptune (Dietrich et al. 2017) can be conducted by AtmoFlow.

Differential Rotating Case

The basic *spherical Couette flow* consists of a rotating inner shell and a fixed outer shell. In the context of this setup the excitation of inertial modes (Kelley et al. 2010; Rieutord et al. 2012) will be studied for the Rossby number range of $-4 < Ro < 4$. Limitations are only given by high Ekman numbers, which are caused by the small outer radius. In geophysics, *differential rotation* plays an important role, when a solid planetary core rotates with a different rate than the surrounding atmosphere or mantle. It produces internal mixing, which proceeds on dynamical time-scales, Maeder (1995). For instance, the inner core of the Earth is assumed to super-rotate with 1° per year, Waszek et al. (2011). Comparable situations are found in Mercury, Jupiter, Earth's moon and Galilean moons. Hereby, the Richardson criterion (Ri > 0.25) parameterizes the condition whether the shear instability is dominant over e.g. buoyancy driven instabilities, or not. For the case of thermo-EHD this criterion is not tested and still an unsolved problem.

## Brief Description of the Experiment

The development of the AtmoFlow experiment benefits from the heritage of the GeoFlow experiments that were performed between 2008 and 2016 in the Fluid Science Laboratory on the ISS. Similarities in the setup are apparent, such as the rotating spherical gap geometry, the central dielectrophoretic force field, and various diagnostic and analytical methods. In particular, AtmoFlow will utilize the same visualization techniques as GeoFlow albeit with some additional and/or modified functionalities. Currently, as of 2018, the AtmoFlow experiment payload is in Phase A/B and the focus of the development work is on the systematic identification and assessment of requirements and consolidation of the concept. The current development baseline assumes accommodation of the payload within the European Drawer Rack Mk II (EDR2, see Fig. 2 and www.esa.int), which should be launched to the ISS and installed in the European Columbus module in the near future.

The ISS provides a microgravity environment that is adequate for the purpose of this experiment. Other microgravity platforms (e.g. drop tower or sounding rockets) are not considered as it is expected that the duration of a single experiment point must last around an hour, which corresponds to the double of a thermal time scale. EDR2 provides interfaces for payloads in terms of mechanical accommodation, access to the stations water cooling loop, various data communication methods, power supply, etc. The concept for the AtmoFlow payload currently consists of a hermetically sealed payload that contains the entire setup including auxiliary systems that are required to perform the experiment. The core of the payload is the fluid cell (see Fig. 3), which is composed of an inner sphere (diameter 0.0378 m), an outer sphere (diameter 0.054 m) and a cooling shell.

The gap between the inner sphere and the outer sphere is filled with the test liquid 3M^{TM}Novec^{TM} 7200 and represents the region of interest for the acquisition of science data. Local temperature boundary conditions are imposed on the poles by cooling plates in the outer shell and at the equator of the inner shell. The mean temperature in the intermediate regions is obtained by a thermalization circuit. Figure 4 depicts the temperature distribution at both shells. A detailed list of all geometrical aspects and the fluid properties is presented in Table 1.

Sensors are located throughout the fluid cell to monitor the temperatures of the thermalization zones and within

Fig. 2 **a** accommodation of
AtmoFlow payload in EDR2, **b**
payload with rotating carousel
(red) and spherical gap unit
(purple). source: Airbus Defence
and Space

a)   b)
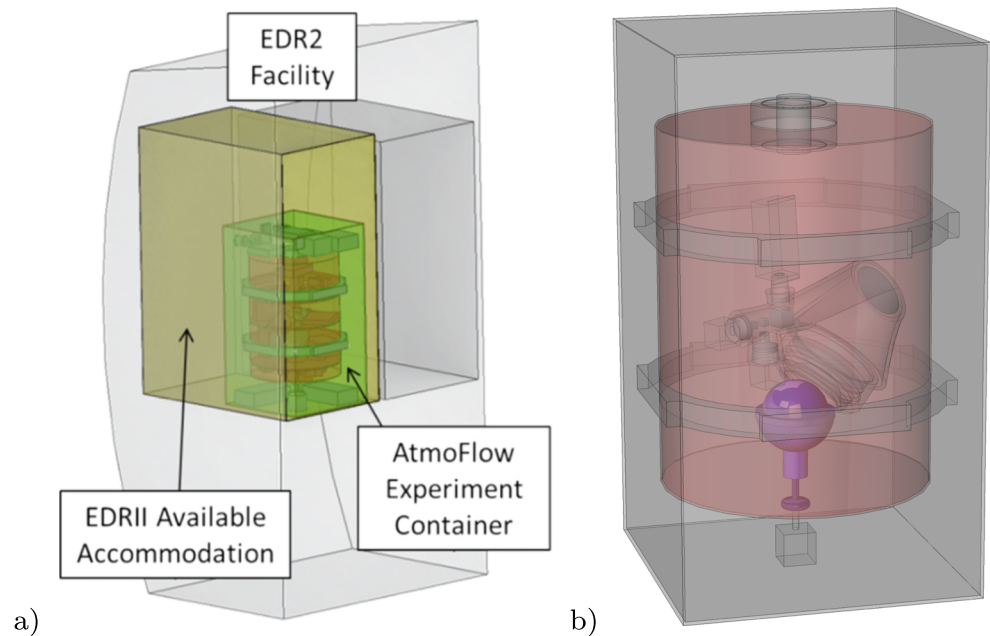
the gap between the cooling shell and the outer sphere.
The inner sphere and the outer sphere also function as
the electrodes for alternating high voltage electrical field,
which generates the dielectrophoretic force on the liquid in
the spherical gap to simulate a planet's gravity. Here, we
refer to Section "Thermo-Electro Hydrodynamics" where
details about the radial force generation are presented.
The entire fluid cell is supported by a rotating carousel
that imposes the rotational velocity Ω_2. In addition, the
inner sphere can be rotated by a separate drive unit
(Ω_1) to impose a differential rotation boundary condition.
Visualization of the fluid phenomena is performed using
shearing interferometry, see e.g. Zaussinger et al. (2017).
The entire optical setup co-rotates with the outer sphere and
observes the test section in a circular region between the
polar region of the upper hemisphere and the equator of
the inner sphere. The field of view stretches across 80° of
the northern hemisphere. The metallic surface of the inner
sphere acts as a mirror in the optical path while the outer
sphere and the cooling shell are transparent in the field
of view. Local temperature gradients cause changes in the
refractive index of the liquid in the optical path which in turn
are visualized as fringes in the resulting interferograms. A
dual camera setup including a beam splitter and dedicated
Wollaston prisms allows for simultaneous interferometry
in perpendicular planes. In addition to the fluid cell,
the payload must accommodate all subsystems that are
required to perform the experiment such as avionics and
power distribution, cooling and thermalization, mechanical
structure and mechanisms, optical diagnostics, actuators and

drives, etc. A data downlink function ensures that the images
acquired by the interferometer cameras and data acquired
by the various sensors within the experiment setup are
transferred to ground for analysis.

Geometry and Thermal Boundary Conditions

The experimental cell, depicted in Fig. 3, will rotate as a
complete assembly and the inner sphere will be equipped
with an additional drive unit to rotate relative to the
experimental cell. The geometry and dimensions of the
experiment cell are defined to fulfill the objectives stated in
Section "Objectives and Scientific Program". The radius of
the outer sphere R_2 is determined by the size and weight
of the optical setup as well as the optical accessibility. This
trade-off leads to a radius of outer sphere at $R_2 = 0.027$ m,
a radius of inner sphere at $R_1 = 0.0189$ m, resulting in a
radius ratio of $\eta = R_1/R_2 = 0.7$. The radius of the inner
sphere is further chosen to reach a radius ratio in between
thin and thick atmospheres.

The key feature of AtmoFlow is the thermal boundary
condition. Realistic atmospheric boundary conditions are
very complex, however, it is possible to break them down to
follow three regions: a) a solar-heated equatorial region with
absorption of re-radiated infrared radiation; b) heat sinks
in the upper atmosphere of the poles and mid-latitudes, c.f.
Chan and Nigam (2009); c) moderate temperature regions
between the polar and the equatorial regions. Imposing these
idealized boundary conditions results in a global circulation,
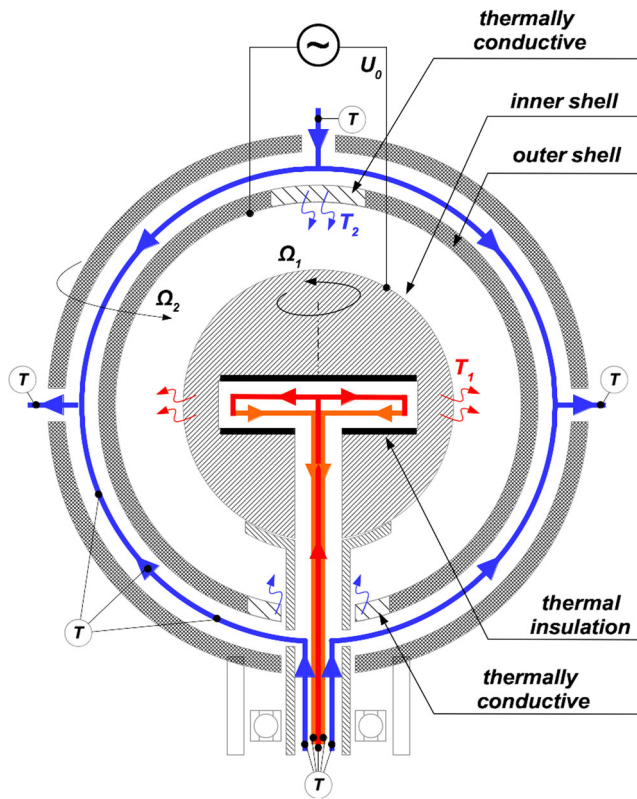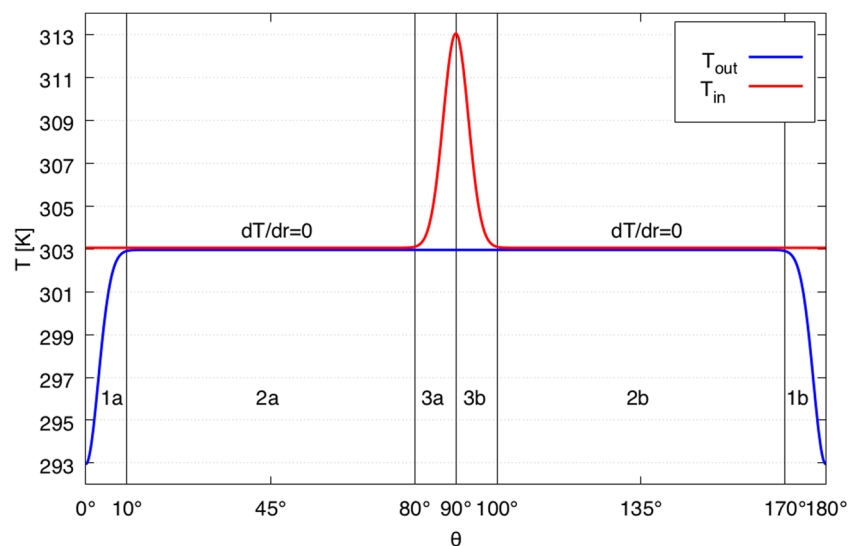which is convectively unstable in the tropics and stable in

Fig. 3 Vertical cut through the AtmoFlow experiment. Blue lines depict the cooling loop, red lines show the heating circuit. Inner and outer rotation is labeled by Ω_1 and Ω_2, respectively. The maximum temperature is found at the equator T_1, the minimum temperature at the poles T_2.

the mid-latitudes. Hence, the heat transfer from the tropics to the stably stratified mid-latitudes and sub-tropics can be investigated with this setup. A baroclinic wave tank with the same specifications has been investigated by Scolan and Read (2017). They observed the interaction and coexistence

of convective and baroclinic zones. Hence, this experiment can be used as validator to study equilibrium processes as they occur in planetary atmospheres. For AtmoFlow the thermal boundaries are imposed by heating plates and cooling loops, which results in Dirichlet type boundary conditions as depicted in Fig. 4. Convection is controlled by varying the temperature at the outer shell. Dielectric heating (see Section "Dielectric Heating") does not change the temperature at the boundaries as it acts only on the fluid in the spherical gap and not in the cooling loops. The temperatures at the boundaries are controlled by thermal sensors. See Section "Temperature Measurement" for a detailed description of the thermal measurements.

The idealized thermal boundary condition used for the numerical simulations represents a conductive solution, when the equator is heated, the upper polar region cooled and the mid-latitudes are insulated. It's the same approach as found in Scolan and Read (2017). Figure 4 depicts these regions in terms of the temperature as function of the lateral angle θ for the maximum temperature difference between the poles and the equator of 20 K, which are used for the accompanying numerical simulations. The imposed thermal distribution at the surface T_{in} and the upper shell T_{out} can be approximated by,

$$T_{out}(\theta) = \frac{T_{hot} + T_{cold}}{2} + \frac{T_{hot} - T_{cold}}{2} \sin^n(\theta) \quad (1)$$

$$T_{out}(\theta) = T_{cold} + \frac{T_{hot} - T_{cold}}{2} \frac{\cosh(A\cos(\theta)) - \cosh(A)}{1 - \cosh(A)}. \quad (2)$$

Here, $\theta = 0°$ is the north pole and $\theta = 180°$ is the south pole. The constant factor $A = 50$ increases the temperature at the poles from T_{cold} to $\frac{T_{hot} - T_{cold}}{2}$ within $\theta = 10°$, see Fig. 4 regions 1a, 1b. In the following, the reference temperature is defined at the equator, $T_{ref} = T_{hot} = 313$ K. All

Fig. 4 Imposed thermal boundary conditions used for the numerical simulations of the AtmoFlow experiment for a maximum temperature difference of 20 K. T_{in} specifies the temperature at the inner shell, T_{out} at the outer shell

Table 1 Geometrical parameters and fluid properties for 3M^{TM}Novec^{TM} 7200 (at 313 K, 10^5 Pa and 10^4 Hz frequency)

parameter	symbol	unit	value
inner radius	R_1	m	1.89×10^{-2}
outer radius	R_2	m	2.7×10^{-2}
radius ratio	η	-	0.7
min. temperature	T_{min}	K	293
max./ref. temperature	T_{max}, T_{ref}	K	313
temperature difference	ΔT	K	$(T_{max} - T_{min})/2$
rotation rate	$\Omega_{1,2}$	Hz	0-2
max. voltage	U	V	10^4
high voltage frequency	f_{HV}	Hz	10^4
kinematic viscosity	ν	m^2/s	3.68×10^{-7}
thermal conductivity	k	W/(mK)	6.61×10^{-2}
spec. heat capacity	c	J/(kg K)	1.241×10^3
thermal diffusivity	κ_T	m^2/s	3.83×10^{-8}
thermal exp. coefficient	α_T	1/K	1.6×10^{-3}
electric exp. coefficient@10.000Hz	α_E	K^{-1}	1.383×10^{-3}
density	ρ	kg/m^3	1.389×10^3
boiling point	T_{boil}	K	349
relative permittivity	ϵ_r	F/m	7.4
loss factor	$\tan \delta$	-	9.73×10^{-2}
refractive index@293K	n	-	1.281

dimensionless numbers refer to this value. The reference length scale is the gap width d = 0.0081 m, the reference temperature difference $\Delta T = T_{ref} - T_m$, where the intermediate temperature is defined as $T_m = \frac{T_{hot} - T_{cold}}{2}$. The width of the temperature peak at the equator T_{hot} is controlled by the factor n=100 and covers 20°, see Fig. 4 region 3a, 3b. Regions except the poles (outer shell regions 2a, 3a, 3b, 2b) and except the equator (inner shell regions 1a, 2a, 2b, 1b) are thermally insulated (dT/dr = 0), see Fig. 4. Due to the insulating regions, the gradient of the permittivity has a non-zero value, which enables the dielectrophoretic force field everywhere in the fluid cell. The specific thermalization of the fluid is realized by two individual cooling/heating circuits, which are integrated in the experimental container.

Working Fluid

The working fluid plays a crucial role and has to fulfill various functions. First, the electric permittivity needs to be as high as possible. This benefits the acceleration based on the dielectrophoretic effect as the voltage can be lowered. Second, the viscosity needs to be low which supports comparisons with realistic atmospheres and water tank experiments. The test liquid requires specific properties especially when used onboard of the ISS in a high voltage environment. It has to be non-flammable, non-toxic, insulating and thermally and chemically stable. Next to silicone oils, per-fluorinated compounds are possible candidates satisfying these requirements. The primary candidate is 3M^{TM}

Novec^{TM} 7200 (ethoxy-nonafluorobutane) $C_4F_9OC_2H_5$. It is a clear, colorless and low-odor fluid. Furthermore, the viscosity is comparable to water Pr(40 °C) = 9.61. Water would be also a candidate with its much larger permittivity as 3M^{TM} Novec^{TM} 7200. However, it is not suitable for long-duration TEHD-experiments since even small amounts of ions coming from e.g. the fluid loop materials dissolute in the ultra-pure water and increase the electrical conductivity drastically.

Experimental Methods and Diagnostics

Interferometry

The direct data analysis methods will be based on the interferograms (Dubois et al. 1999; Egbers et al. 2003; Zaussinger et al. 2017) and telemetry data (Jehring et al. 2009) and consist of the following aspects:

– Tracking and recognition of convective flow pattern using image processing tools.
– Calculation of the mean temperature field using two perpendicular orientated interferometric images.

The indirect analysis methods are based on a comparison of the experimental results with numerical simulations. Hereby, numerical simulations are performed with identical conditions, whose results can be converted into artificial interferograms. If the interferograms match qualitatively,

the flow state can be analyzed in much more detail with respect to the determination of the temperature field and the three dimensional velocity field, including cell-formation, turbulence, interaction of planetary waves, statistics and extreme value analysis.

The methods described above have already been developed and applied to the GeoFlow experiment data with great success (Egbers et al. 2003; Zaussinger et al. 2017) and is being modified and applied to the AtmoFlow parameters in a separate scientific program funded by DLR Space Administration.

To investigate the flow in the gap between the inner and outer sphere, a Wollaston Shearing Interferometer (WSI) shall be used, which co-rotates with the outer sphere. As minimum field of view, an angular region of 80° between the north pole and the equator is required. To enable measurements of the density gradient in two perpendicular directions simultaneously, the illuminated flow shall be recorded with two cameras each outfitted with a dedicated Wollaston prism. The cameras should have a minimum image acquisition frequency of 1 fps (exposure time 1/500 s), a minimum image dynamic range of 8 Bit grayscale and a minimum optical resolution of 1024x1024 px, which leads to 10 px per fringe in the interferograms.

The triggering of the cameras will be synchronized with the inner sphere, which therefore would require an image acquisition frequency higher than 1 fps. As the cameras are co-rotating with the outer sphere, markers are required on the inner sphere within the field of view, to determine the relative position of the inner and outer sphere in the recorded images. This allows to track and measure convective structures in post processing tools.

The illumination of the flow shall be realized by a laser light source, whose intensity will be variable by command uplink and whose wavelength has to be optimized for use with the materials in the optical path. A possible solution is a wavelength of 532 nm. Further, the Wollaston prisms will allow to record two interferograms simultaneously. The sensitivity of the interferometer strongly depends on the temperature gradient inside the field of view and has to be determined within ground experiments, see Section "Laboratory Experiments".

Experimental Runs and Data Handling

To capture the whole parameter space, experimental points are defined. They can be divided into one non-rotating scenario, three rotation scenarios (15 values solid body rotation, 10 values differential rotation at low rotation, 10 values differential rotation at high rotation) and by 20 different electric Rayleigh numbers Ra_E. In total, 12

experimental runs are defined which account for 720 experimental points. Each run has a duration of 60 min which results in $1024^2 \times 1$byte $\times 1$fps $\times 3600$s $\times 720$ EP $= 2.7$ TB of image data. The amount of telemetry data is low compared to images and does not contribute much to the total amount of data.

Temperature Measurement

In the AtmoFlow experiment, temperature measurements are needed to monitor the thermal boundary conditions. Therefore, the temperature has to be recorded near the poles of the outer sphere, near the equator of the inner sphere and in the southern or northern half sphere of the cooling liquid volume outside the field of view of the optical diagnostics. In the latter case, three sensors at $\theta = 22.5°$, $\theta = 45°$ and $\theta = 67.5°$ are sufficient. In addition, the temperature is monitored in the outflow region of the cooling liquid volume. The installed temperature sensors will have a temperature range of 283 K $- 353$ K, an accuracy of 0.2 K (poles and equator), 0.5 K (north or south hemisphere) and a frequency of 1 Hz.

Velocity Measurement

Common techniques to measure fluid velocities are digital holographic velocimeter (Prodi et al. 2006), Particle Image Velocimetry (Meier et al. 2018) and Laser Doppler Anemometry. However, particles for these methods need special treatment or would require the involvement of astronautical staff members. Furthermore, difficulties in connection with tracer based diagnostics in a high voltage environment are assumed. In summary, no direct velocity measurements will be performed. The velocity field will be reconstructed by comparing interferograms with numerical simulations. This has been performed successfully for GeoFlow II as demonstrated in Zaussinger et al. (2018b).

Acceleration Measurement

Long time scale and diffusion driven experiments under microgravity conditions depend on the g-jitter. Trajectories show loops and can cause trembling, see e.g. Shevtsova et al. (2004). To capture these uncertainties acceleration measurements are required. The ISS provides two systems, the Space Acceleration Measurement System II (SAMS-II) and the Microgravity Acceleration Measurement System (MAMS), see e.g. Jules et al. (2004) and Rice et al. (1999), respectively. However, to capture acceleration events near the payload these measurements will be done independently from the mentioned accelerometers near by the experiment in three directions with an accuracy of 10^{-5} g_0 and an

acquisition rate with at least doubled image acquisition frame rate. Hereby, a frequency range of 5 to 100 Hz is covered. The acceleration amplitude is averaged over a duration of one second. The quality of microgravity shall be better than 10^{-3} g_0 during the collection of the science data at all experimental data points.

Laboratory Experiments

Within the AtmoFlow project, a laboratory experiment is planned in the so-called 'baroclinic wave tank' facility at the BTU Cottbus-Senftenberg, which can give reasonable results for the flow in the mid-latitudes of a spherical shell (Vincze et al. 2015). Thereby, basic flow phenomena like the baroclinic instability can be analyzed on Earth. While the space experiments are restricted to the use of the Wollaston Shearing Interferometry (WSI), in the wave tank setup, we can combine the WSI technique together with Infrared-thermography (IR). Accordingly, the aim of the experiments in the baroclinic wave tank is to characterize specific interference pattern in the parameter space of the AtmoFlow project. Especially interferograms of waves are in the focus of this experiment. So far, only convective patterns like sheet-like upwellings or steep downdrafts can be identified clearly in the with Wollaston shearing interferometry, Zaussinger et al. (2017). The baroclinic wave tank gives the possibility to develop post-processing routines which can be used to identify waves and related wave numbers. Furthermore, interferograms depicting the interaction of convection and waves can be identified clearly using further imaging methods. The tank will also be used to calibrate the interferometry unit for AtmoFlow. Interferograms of the GeoFlow experiment showed many artifacts, which increased the post-processing. Testing the interferometry unit on the baroclinic wave tank will reduce the risk of interferograms with reduced quality.

Table 2 Geometrical and experimental parameters of the baroclinic wave tank experiment

parameter	symbol	unit	value
radius inner cylinder	R_{1c}	m	0.45
radius outer cylinder	R_{2c}	m	0.12
fluid height	H	m	0.135
angular velocity	Ω	rpm	0.1-30

A database of common flow patterns consisting of IR images, interferograms and numerical simulations is planned. This database will be the basis for the post-processing phase of AtmoFlow, where machine learning algorithms are trained on reference patterns. Furthermore, an algorithm will be developed to reconstruct the average temperature field from the interference images by use of the additional IR data. The proposed ground experiment is depicted in Fig. 5.

The baroclinic wave tank consists of two concentric cylinders, which are mounted on a rotation table. The measurement gap between the cylinders is filled with distilled water, which has comparable Prandtl number of the AtmoFlow working fluid 3M™ Novec™ 7200. The inner cylinder is made of anodized aluminum and the outer one of borosilicate glass. While the bottom end of the experiment is enclosed by an opaque end plate, the top side has a free surface. The outer cylinder is surrounded by a second borosilicate glass cylinder, which is filled with distilled water and equipped with heating coils. Thus, the outer cylinder can be heated. Further, the inner cylinder features cooling channels and is cooled via a thermostat. Therefore, a radial temperature gradient adjusts with an accuracy of ± 0.1 K/m. The angular velocity of the rotation table as well as the temperatures of the cylinders are controlled by LabView©. The geometrical parameters of the baroclinic wave tank are summarized in Table 2. To enable

Fig. 5 Sketch of the g_0 experiment 'baroclinic wave tank' and the planned set up of the measurement technique, which is considered in the AtmoFlow experiment
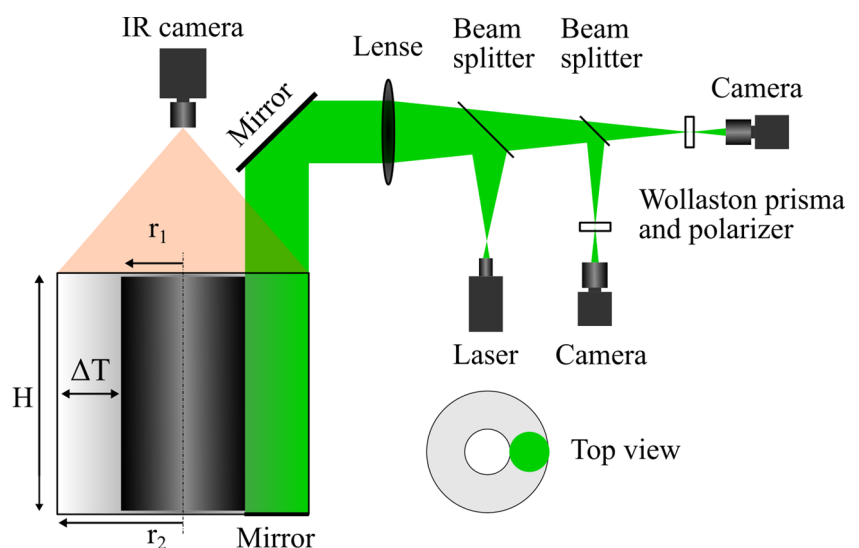
simultaneous measurements of WSI and IR thermography, the experiment is revised. The upper end of the experimental gap is enclosed by an IR transparent top plate, to prevent possible surface waves, which would distort the interference images. Furthermore, the IR camera as well as the WSI components are mounted with a stiff connection to the turn table of the experiment in order to measure in a co-rotating frame. Data and power supply connections are realized by means of a slip ring.

The WSI set up consists of a laser beam ($\lambda = 532$ nm), which is expanded to cover a circular area of 80 mm^2, and enters into the measurement gap through the top plate. At the bottom of the experiment the laser beam is reflected and split into two beams. These two light beams are captured by two cameras, each equipped with orthogonal oriented Wollaston prisms and a polarizer. The Wollaston prisms cause an interference of light rays, separated by the distance e. The focal length f of the lens collimating the light beam at the prism and the separation angle of the prism α define the ray distance $f \tan \alpha$. The light intensity distribution I of the interference images is a function of the local gradient of refractive index n in the direction $\mathbf{s}$ of the Wollaston prism orientation which is strongly temperature dependent. The intensity variations in $\mathbf{s}$-direction are obtained by

$$\frac{\Delta I}{I} = \cos \left(\frac{2 \pi e}{\lambda} \frac{\partial n}{\partial \mathbf{s}} \right). \tag{3}$$

In the following, we demonstrate the reconstruction of the temperature field by the usage of two perpendicular WSI

units. This example is based on a temperature measurement of the baroclinic wave tank with a gap width of 0.1 m, at 214 rpm and a temperature difference of 9 K between the inner and outer shell, see Fig. 6. Numerical interferograms are calculated by Eq. 3 for the x-direction and the y-direction, see Fig. 6a and b, respectively. Combining both interferograms reveals the global structures as found in the temperature field, see Fig. 6c, d. The same approach is considered for the AtmoFlow experiment, where two interferograms will be captured simultaneously.

Thermo-Electro Hydrodynamics

Dielectrophoretic Effect

The force $\mathbf{F}$ of the electric field exerting on the fluid is given by the Coulomb force $\mathbf{F}_C$, the electro-strictive force $\mathbf{F}_{ES}$ and the dielectrophoretic force $\mathbf{F}_{DEP}$,

$$\mathbf{F} = \underbrace{\rho_V \mathbf{E}}_{\mathbf{F}_C} + \underbrace{\nabla \left[\frac{1}{2} \rho \left(\frac{\partial \epsilon}{\partial \rho} \right)_T \mathbf{E}^2 \right]}_{\mathbf{F}_{ES}} - \underbrace{\frac{1}{2} \mathbf{E}^2 \nabla \epsilon}_{\mathbf{F}_{DEP}}. \tag{4}$$

The working fluid 3M^{TM} Novec^{TM} 7200 does not carry free charges, resulting in $\mathbf{F}_C = 0$. Furthermore, the electro-strictive pressure force $\mathbf{F}_{ES} = \nabla p_{ES}$ does not contribute to the flow field in the incompressible formulation and is combined with the pressure, Castellanos (1998), Mutabazi

Fig. 6 Numerical interferograms calculated for the temperature distribution in a baroclinic wave tank in **a** the x-direction and **b** the y-direction. **c** combination of both interferograms, **d** experimental temperature distribution used for the calculations. Data provided by Früh (2018)
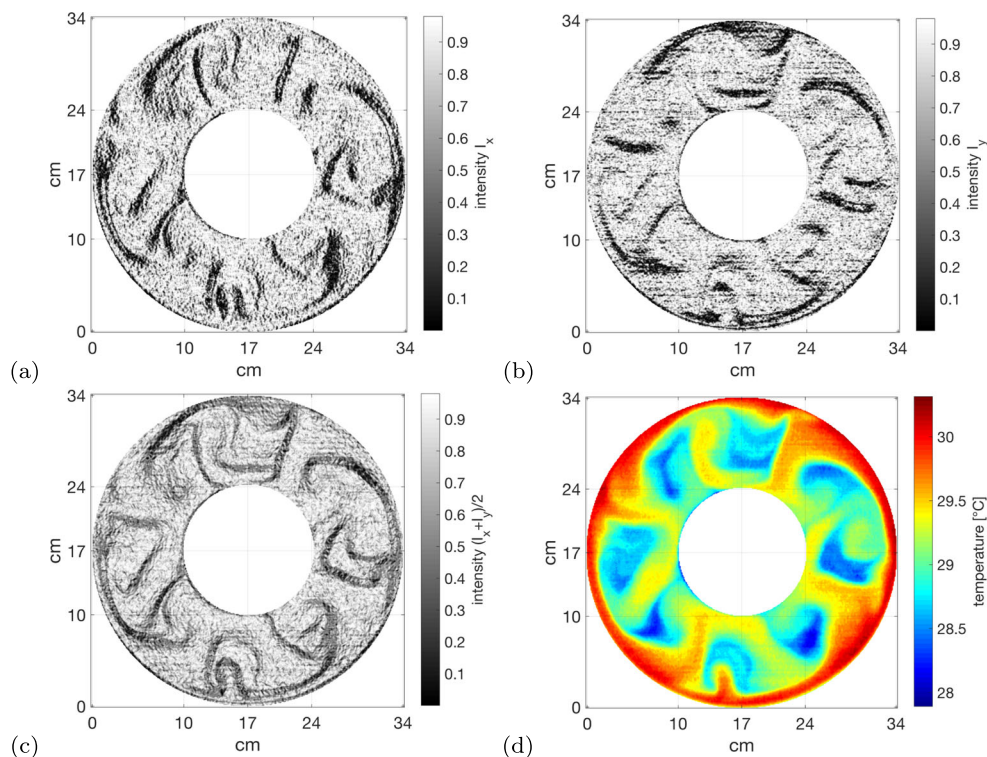
et al. (2016). The dielectrophoretic force of a spherical capacitor with hot inner shell and cold outer shell is mainly radial directed **r**. Horizontal components are about five magnitudes smaller than the radial component and are neglected in the following. This enables a radial acceleration field called *electric gravity*,

$$\mathbf{g_E} = \frac{\alpha_E}{\rho_0 \alpha_T} \nabla \left(\frac{\epsilon_0 \epsilon_r \mathbf{E}^2}{2} \right). \tag{5}$$

For homogeneously thermalized boundaries (T_1 inner shell, T_2 outer shell) it has (or assumes) its maximum $|\mathbf{g_E}| = 3.82$ m/s^2 for $U_{rms} = 5$ kV at the inner shell and its minimum $|\mathbf{g_E}| = 0.15$ m/s^2 for $U_{rms} = 1.0$ kV at the outer shell, respectively, see Fig. 7a. The magnitude of the acceleration $\mathbf{g_E}$ depends on the electric properties of the fluid and the geometry. The direction of the electric gravity is mainly determined by the gradient in the temperature dependent electric permittivity $\epsilon = \epsilon_0 \epsilon_r$, where ϵ_0 is the vacuum permittivity and ϵ_r is the relative permittivity $\epsilon_r(T) = A \cdot T^2 + B \cdot T + C$ and $A = 7.1429 \times 10^{-4}$, $B = -5.1103 \times 10^{-1}$ and $C = 9.7467 \times 10^2$. This function is a second order polynomial approximation to a measurement provided by Airbus Defense and Space. The electric expansion coefficient α_E and the thermal expansion coefficient α_T are available by measurements, too. The direction of the electric gravity coincides with the temperature gradient in the defined temperature regime.

Microgravity conditions are required due to the low acceleration at the outer shell, which is much lower than the Earth's gravity. The corresponding *electric Rayleigh number* is obtained by,

$$Ra_E = \frac{\alpha_T \, g_E \, \Delta T \, d^3}{\nu \kappa_T}. \tag{6}$$

where $\Delta T = (T_{ref} - T_{min})/2$ and $d = R_2 - R_1$. This Rayleigh number is defined for $R_1 = 0.0189$ m at constant equatorial temperature of $T_{ref} = 313$ K. It covers about three magnitudes, $2.47 \times 10^3 < Ra_E <$

6.17×10^6, see Fig. 7b. All transitions between conductive, laminar and turbulent flows are observed in this parameter range. Additionally, the parameter range is accessible by accompanying direct numerical simulations.

Furthermore, two dimensionless numbers corresponding to rotation are introduced. The Taylor number,

$$Ta = \left(\frac{2 \Omega d^2}{\nu} \right)^2 \tag{7}$$

ranges between $2 \times 10^1 < Ta < 2 \times 10^7$, see Fig. 8a. The Rossby number is a dimensionless number parameterizing differential rotation,

$$Ro = \frac{\Omega_1 - \Omega_2}{\Omega_2} \tag{8}$$

and ranges between $-3.59 < Ro < 3.59$, see Fig. 8b.

Dielectric Heating

Dielectric heating plays a crucial role for the fluid flow which is under the influence of an a.c. electric field. The microwave stove is based on this physical process causing water molecules to rotate and releasing heat at a frequency of 2.45 GHz. The same situation occurs for the polar working fluid 3M^{TM} Novec^{TM} 7200. The heating as function of the electric field strength is higher at the inner shell than at the outer shell. It scales with the square of the electric field strength and linearly with the frequency of the electric field, see e.g. Zaussinger et al. (2018b). The rate of dielectric heating S_{DH} [K/s] is obtained by,

$$S_{DH} = \frac{2\pi f_{HV} \epsilon_0 \epsilon' \tan \delta |\mathbf{E}|^2}{\rho C_p}. \tag{9}$$

where ϵ' is the real part of the relative permittivity and $\tan \delta$ is the dielectric loss rate. Both values are obtained by measurements. In the following, we show the impact of dielectric heating on the temperature distribution in the case where the boundaries are kept isothermally (Fig. 9a), for an

Fig. 7 **a** electric gravity g_E as function of high voltage at the inner shell and out shell, respectively. **b** electric Rayleigh number Ra_E as function of temperature difference
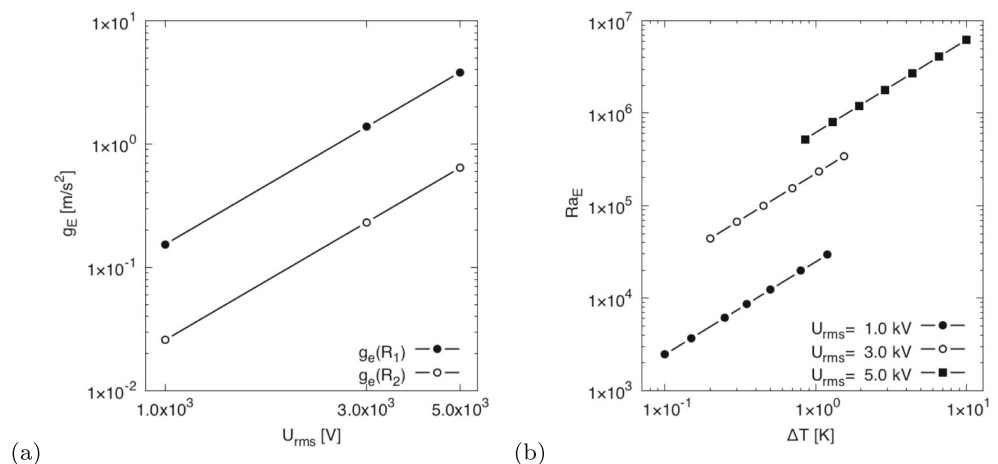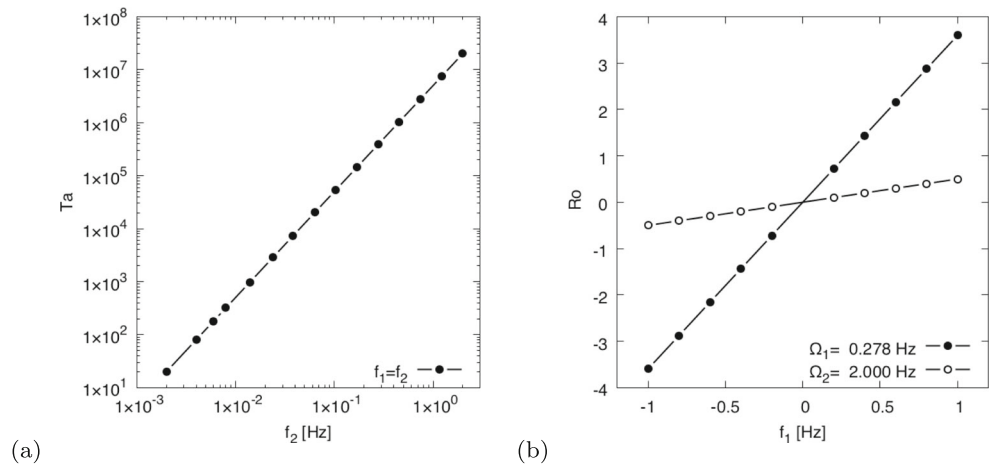
Fig. 8 **a** Taylor number Ta as function of inner shell rotation rate Ω_2. **b** Rossby number Ro as function of the rotation rates Ω_1 and Ω_2

(a)   (b)

applied temperature contrast (Fig. 9b) of $\Delta T = 10$ K and various high voltages U_{rms}. The temperature profile in the stationary case can be described by a parabola shape, where the peak value is in the bulk and not at the boundaries. The parabola profile of the temperature distribution reaches its final shape within one thermal time scale ($\tau = 1713$ sec). It is found that the peak value is stationary as depicted in Fig. 10 for various voltages. The boiling point of the working fluid is 349 K. This allows a maximum difference between the reference temperature and the maximum of the temperature due to dielectric heating of $|?? - ??_{ref}| = |249 - 313| = 36\,K$. The highest temperature found with dielectric heating is $|T - T_{ref}| = 29\,K$ for $U_{rms} = 5.0$ kV. This is seven degrees lower than the boiling temperature. In case of isothermally heated boundaries the maximum temperature due to dielectric heating is about 20 degrees below the boiling point. Based on these calculations it is

considered to limit the voltage to $U_{rms} = 5000$ V and the frequency to f$\leq 10^4$ Hz.

Numerical Simulations

Accompanying numerical simulations are performed for the AtmoFlow experiment. They are used to reconstruct the velocity field, which is not accessible by measurement techniques used in AtmoFlow. The reconstruction is based on a comparison of experimental and numerical interferograms. Matching structures in both interferograms correlate with similar temperature and velocity fields. Based on this assumption, the three-dimensional fluid flow gets accessible. However, drift velocities of convective structures are used to support the comparison. Drift rates are calculated directly from interferograms by identifying markers and
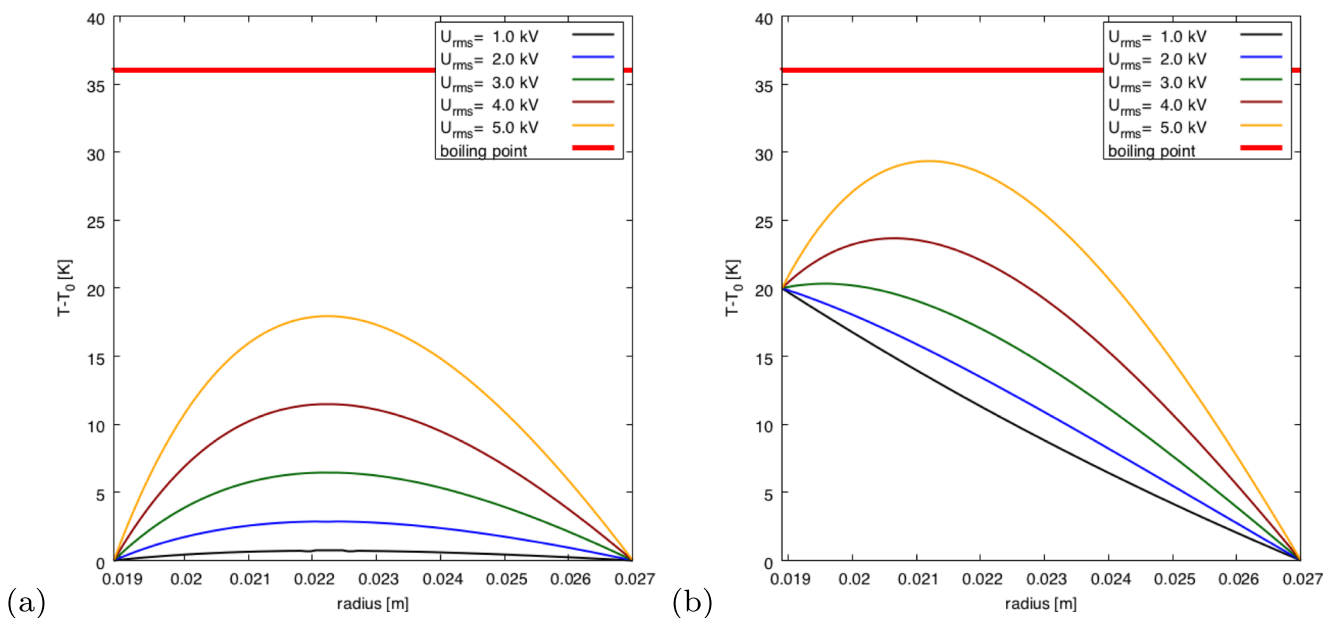

(a)   (b)

Fig. 9 Conductive thermal distribution in the spherical gap under the influence of dielectric heating for $f_{HV} = 10.000$ Hz and $T_{ref} = 313$ K for the case of **a** an iso-thermal case and **b** a temperature contrast of 20K between the inner and the outer shell

Fig. 10 Temporal evolution of the thermal peak value T_{max} near the middle of the gap for $f_{HV} = 10.000$ Hz and $T_0 = 313$ K. (inlet) temperature peak T_{max} as function of voltage
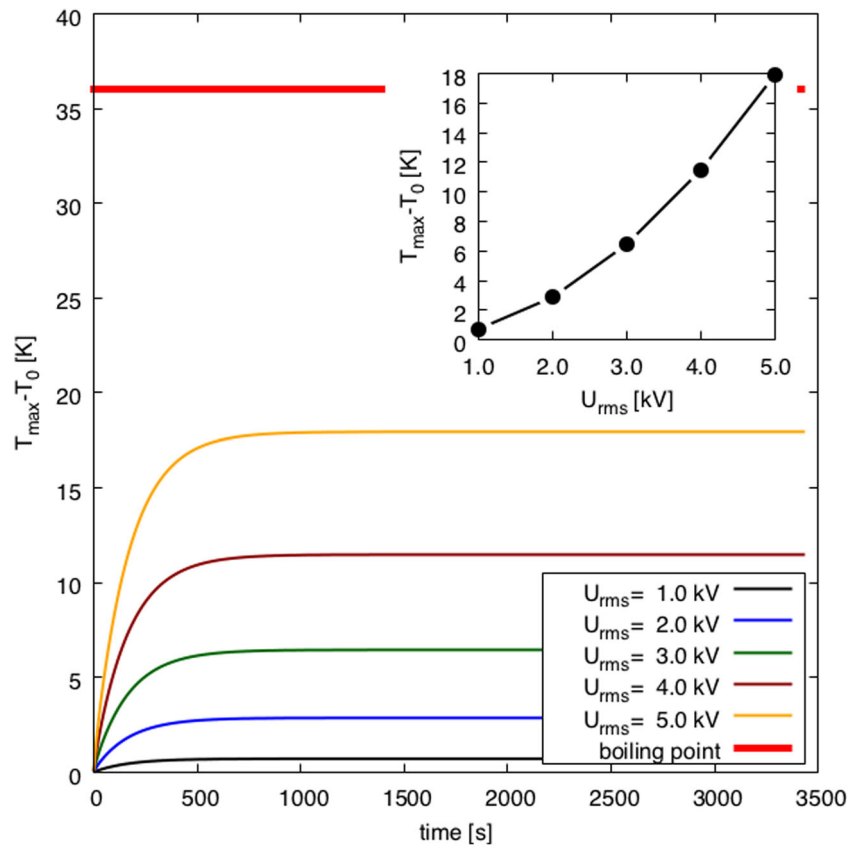
slowly moving convection cells. They have to be identical in the numerical simulations and in the experiment. In principle, the parameter range of AtmoFlow can be captured by direct numerical simulations. However, they cannot replace the experiment. This is based on the thermo-EHD model, which has still many open questions, Mutabazi et al. (2016). It is e.g. unclear if the Boussinesq approximation is valid for dielectrophoretic driven convection, when temperature differences exceed 3 K. Additionally, dielectric heating has been identified as important term in the model, which is under active research. AtmoFlow shall be used as validator for physical models of EHD regarding convection and internal heating. The governing equations are based on the EHD model presented in Section "Thermo-Electro Hydrodynamics" and the conservation equations of fluid mechanics (Platten and Legros 2012). A comprehensive

$$\nabla \cdot \mathbf{u} = 0 \tag{10}$$

$$\rho_0 \frac{\partial \mathbf{u}}{\partial t} + (\mathbf{u} \cdot \nabla)\mathbf{u} = -\nabla p + \nabla \cdot \bar{\bar{\sigma}} - 2\rho_0 \Omega \times \mathbf{u}$$
$$-\rho(T)\Omega \times (\Omega \times \mathbf{r}) + \rho \mathbf{F}_{DEP} \tag{11}$$

$$\frac{\partial T}{\partial t} + (\mathbf{u} \cdot \nabla)T = \kappa_T \nabla^2 T + S_{DH} \tag{12}$$

$$\nabla \cdot (\epsilon(T)\nabla\phi) = 0 \tag{13}$$

$$\nabla\phi = \mathbf{E} \tag{14}$$

$$\nabla \times \mathbf{E} = 0. \tag{15}$$

Here, $\mathbf{u}$ is the velocity field, Ω is the angular velocity vector, $\mathbf{r}$ is the position vector, p is the pressure, $\bar{\bar{\sigma}}$ is the viscous stress tensor, $\rho = \rho(T)$, ρ_0 is the reference density, $\mathbf{F}_{DEP}$ is the dielectrophoretic force, T is the temperature, κ_T is the thermal diffusion coefficient, S_{DH} is the dielectric heating term and ϵ is the permittivity. Fluid properties are provided in tabulated form. The electric field is expressed in terms of the scalar potential ϕ, where $\phi(R_1) = 0$ and $\phi(R_2) = U_{rms}$. This relation results in a non-linear Helmholtz equation which is solved iteratively in each numerical time step,

$$\nabla \cdot (\epsilon(T)\nabla\phi(T)) = 0 \tag{16}$$

The governing equations are solved numerically with the finite volume method (FVM) using the open source software suite OpenFOAM, Weller et al. (1998). A cubed spherical grid with 4×10^6 cells is used for all simulations, where the radial resolution is 60 cells. The velocity boundary conditions are kept no-slip. The thermal boundaries are of Dirichlet type, according Eq. 2. The code solves the governing equations dimensionally in 3D with the PIMPLE algorithm. This algorithm is based on the SIMPLE approach for the solution of incompressible flows, but iterates the pressure loop several times to increase the precision of the solution. The time integration is performed with an implicit Crank-Nicolson method, the space derivatives are approximated in

second order. Turbulent cases in the high Rayleigh number regime are modeled with the one-equation turbulence model 'dynamic-k'. The accuracy of the results is guaranteed by the velocity residual of $< 10^{-6}$. We refer to Zaussinger et al. (2018b) for a detailed description of the numerical setup. The main numerical study consists of 72 numerical simulations which are located in the $Ra_E - Ta - Ro$ parameter space. In the following, three representative simulations with a temperature difference of 20 K between the equator and the poles are presented. The high voltage is set to $U_{rms} = 2800$ V in all cases. Additionally, all fluid properties are interpolated from the fluid's data sheet and temperature dependent. Here, the maximum electric gravity $\mathbf{g}_E = 1.2$ m/s^2 is found at the inner sphere and the minimum $\mathbf{g}_E = 0.2$ m/s^2 at the outer sphere. The corresponding Rayleigh number is $Ra_E = 1.9 \times 10^6$. Rotation is applied in the solid-body rotation case with a rate of $\Omega_1 = \Omega_2 = 0.8$ Hz. In case of differential rotation the inner shell rotates with $\Omega_1 = 0.88$ Hz and the outer shell with $\Omega_2 = 0.8$ Hz, respectively. This results in $Ta = 3.2 \times 10^6$ and $Ro = 0.1$. Hammer-Aitoff projections are calculated using the interpolation program TOMS661 (Renka 1988). Hereby, the Cartesian grid of OpenFOAM is interpolated onto a grid in spherical coordinates with the same amount of data points. For reasons of visibility the temperature and radial velocity are averaged along the radius. The artificial interferograms are calculated by superimposing two orthogonal interferograms, one in

x-direction and one in the z-axis, respectively. The intensity I of the interferograms is calculated according Eq. 3 with fluid properties of the working fluid and specifications of the optical path which have been used for GeoFlow.

Non-Rotating Case

The non-rotation case is depicted in Fig. 11. Besides the equatorial up-welling region and the polar down-welling plumes, the overall temperature field is dominated by small, local plumes. These plumes are spread in a band-like structure along the latitudes. The Hammer-Aitoff projection Fig. 11a and especially the thermal contour lines of the radially averaged temperature highlight this global cell formation. Interestingly, the numerical interferogram in Fig. 11b shows these plumes as alined 'string of pearls' structure. A closer look on the velocity field (not depicted) shows many small vortices spread irregularly over both hemispheres. The only up-welling region is found around the equator. This results in a well mixed temperature field with low gradients.

Solid Body Rotation Case

Figure 12 depicts a representative solid body rotation case. This case reveals new fluid structures, which are based on rotational effects. The overall temperature distribution is

Fig. 11 Numerical simulations of the non-rotation case at time stamp t=5650 sec for $Ra_E = 1.9 \times 10^6$: **a** radially averaged temperature field as Hammer-Aitoff projection, **b** superposition of two orthogonal artificial interferograms
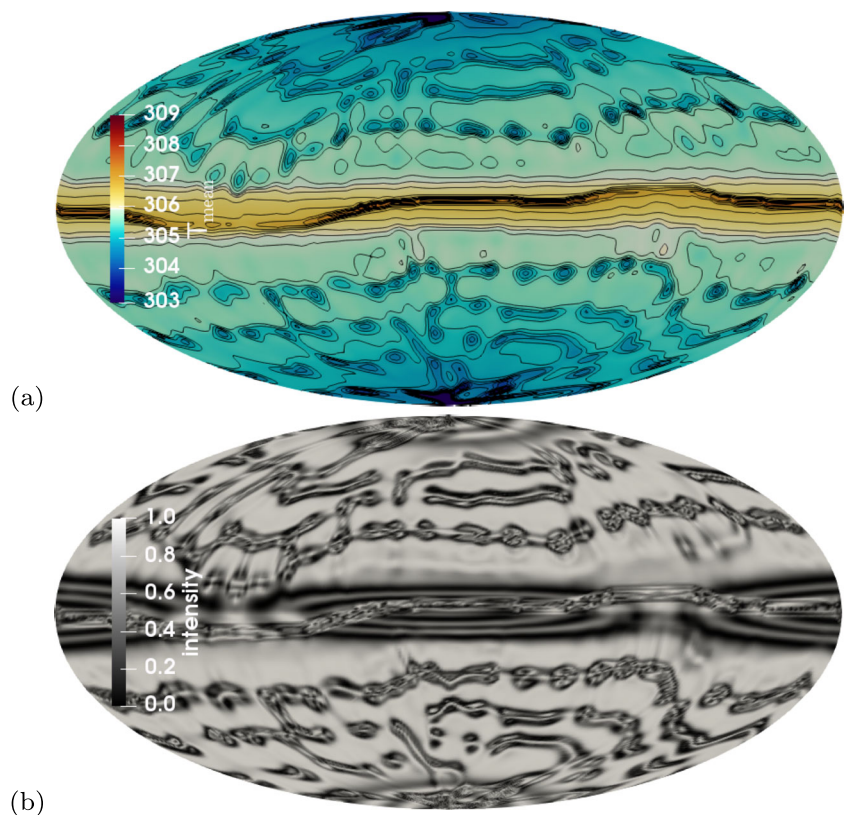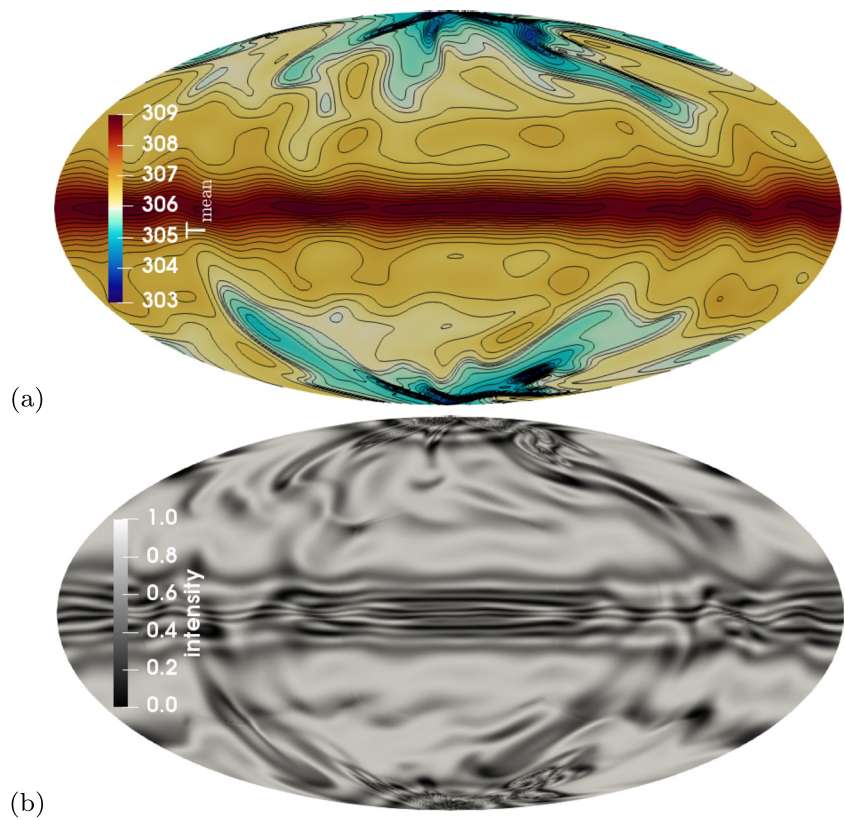

(a)

(b)

Fig. 12 Numerical simulations of the solid body rotation case at time stamp t = 2180 sec for $Ra_E = 1.9 \times 10^6$ and $Ta = 3.2 \times 10^6$: **a** radially averaged temperature field as Hammer-Aitoff projection, **b** superposition of two orthogonal artificial interferograms

(a)

(b)

Fig. 13 Numerical simulations of the differential rotation case at time stamp t=420 sec for $Ra_E = 1.9 \times 10^4$, $Ta = 3.8 \times 10^5$ and $Ro = 0.72$: **a** radially averaged temperature field as Hammer-Aitoff projection, **b** superposition of two orthogonal artificial interferograms

(a)

(b)
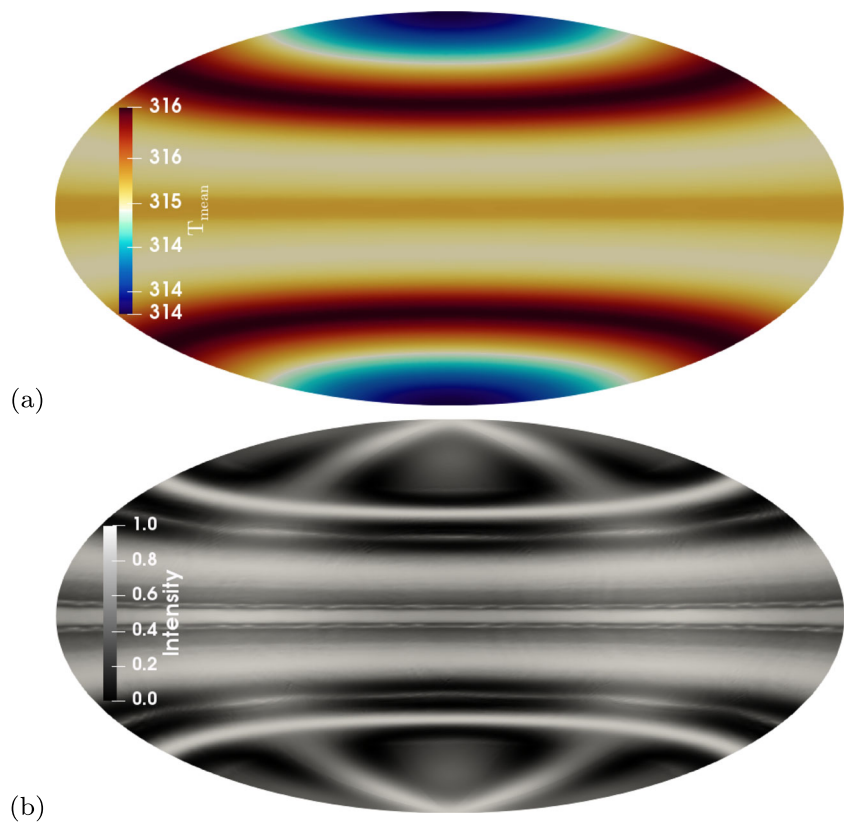
dominated by broad up-welling and down-welling regions at the equator and the poles, respectively. However, in contrast to the non-rotating case only a few large vortices are visible. Local plumes are not found, except in the polar region. The equatorial region reveals a dominant planetary wave with mode m = 9. This wave is visible in the velocity field, the Hammer-Aitoff projection and in the interferogram, too. Hence, this specific simulation can be used as benchmark test for the comparison between the numerical model and the experiment. The poles are characterized by cold fronts reaching deep into the mid-latitudes. These 'fingers' are not symmetrically arranged over both hemispheres, which emphasize the time-dependent and turbulent character of this fluid flow. The interferogram shown in Fig. 12b reveals all mentioned flow structures. Concentric rings at the poles indicate the polar plumes and cold fronts are clearly visible as fringes, too. The equatorial wave can be identified clearly in distorted fringes.

Differential Rotation Case

Figure 13 depicts the case when the inner shell rotates 40% faster than the outer shell. For inner shell rotation $f_1 = 0.278$ Hz and outer shell rotation $f_2 = 0.2$ Hz the Rossby number is Ro = 0.72. The temperature difference of $\Delta T = 0.2$ K and the low voltage if $V_{rms} = 2800\,V$ results in an electric Rayleigh number of $Ra_E = 19400$. Small temperature difference across the gap and low Taylor/Rossby numbers originate in band-like structures and zonal flows as known from gas giants. This specific structure is based on dielectric heating (see temperature legend in Fig. 13a) which dominates the thermal distribution in the bulk. Strong convective flows, aligned with the rotation axis result from the internal heating process. Boundary driven convection is secondary and does not contribute much. The meridional velocity field shows two global thermal plumes in each hemisphere. Furthermore, the interferogram depicted in Fig. 13b reveals these cells. One broad belt in the tropics and one narrow belt in the mid-latitudes.

Conclusions and Outlook

In summary, this paper gives an overview of the current status of the AtmoFlow experiment development. AtmoFlow has been planned for long-term investigation of thermal convection in rotating spherical shells under the influence of a central force field with complex boundary conditions. This setup represents a simplified deep atmosphere as found in giant planets. Microgravity conditions e.g. on the ISS are needed to overcome superpositions of the Earth's gravity and the radial acceleration by the dielectrophoretic

effect. The experiment consists of three main parts: a) two concentric spherical shells filled with the test liquid and thermalized by atmospheric like boundary conditions. b) a rotation tray with two perpendicular co-rotating visualization units, and c) high voltage supply for the radial force field. The payload will be designed for accommodation in the European Drawer Rack Mk II.

Based on the presented parameter space and test matrix, it is intended to investigate approximately 720 individual experiment data points during the scientific test campaign. The data generated from the experiment will be exploited for the following scientific purposes which are related to meteorology, geophysics, astrophysics and engineering:

– The stability of the basic flow states and its transitions with and without rotation
– Interaction of free convection and global wave modes.
– The characteristics of the convective flows and in particular their symmetries.
– Atmospheric cell formation as function of rotation and temperature.
– The critical Rayleigh numbers and wave numbers, which denote linear stability and marks the onset of thermal convection.
– The stability diagram for the different flow states.

The development of AtmoFlow is accompanied by a laboratory experiment and numerical simulations. The baroclinic wave tank experiment is used to evaluate the double interferometry unit and to create a reference database with patterns as they are found in convective fluid flows. Numerical simulations are needed to reconstruct the velocity field, which is not directly accessible by the experiment. Hereby, experimental and numerical interferograms are compared automatically in the post-processing phase of the mission. Stability analysis helps to expound the parameter space, especially the critical dimensionless parameters as the Rayleigh number, the Taylor number or the Rossby number.

Understanding and controlling fluid flow in a spherical geometry under the influence of rotation will be useful in a variety of engineering applications, such as improving spherical gyroscopes, bearings, and centrifugal pumps. Furthermore, study of effects related to the electro-hydrodynamic force, which serves to simulate the central gravity field, will find applications in high-performance heat exchangers, and in the study of electro-viscous phenomena e.g. dielectric heating. Even though fluid properties, geometry and boundary conditions differ in industrial applications, the AtmoFlow experiment may provide useful fundamental research in the dynamics of rotating thermo-EHD devices. It will help to understand the motion of liquids in industrial applications, where e.g. injected ions are a source of charge, e.g. in

EHD-pumps, EHD nozzles, electrostatic precipitators or ion-drag pumps. In summary, it is expected that this experiment will deliver results in fluid mechanics, engineering, geophysics, astrophysics, meteorology and fluid transport.

The AtmoFlow experiment payload is currently in development for operation on the ISS.

Compliance with Ethical Standards

Conflict of interests The authors declare that they have no conflict of interest.

References

Beltrame, P., Egbers, C., Hollerbach, R.: The geoflow-experiment on {ISS} (part iii): Bifurcation analysis. Adv. Space Res. **32**(2), 191–197 (2003). https://doi.org/10.1016/S0273-1177(03)90250-X. http://www.sciencedirect.com/science/article/pii/S027311770390250X, gravitational Effects in Physico-Chemical Processes

Borcia, I.D., Harlander, U.: Inertial waves in a rotating annulus with inclined inner cylinder: comparing the spectrum of wave attractor frequency bands and the eigenspectrum in the limit of zero inclination. Theor. Comput. Fluid Dyn. **27**(3), 397–413 (2013). https://doi.org/10.1007/s00162-012-0278-6

Bronowicki, P., Canfield, P., Grah, A., Dreyer, M.: Free surfaces in open capillary channels—parallel plates. Phys. Fluids **27**(1) (2015)

Busse, F.H., Carrigan, C.R.: Laboratory simulation of thermal convection in rotating planets and stars. Science **191**(4222), 81–83 (1976). https://doi.org/10.1126/science.191.4222.81. http://science.sciencemag.org/content/191/4222/81

Canfield, P.: Stability of Free Surfaces in Single-Phase and Two-Phase Open Capillary Channel Flow in a Microgravity Environment. Cuvillier Verlag, Göttingen (2018)

Canfield, P., Bronowicki, P., Chen, Y., Kiewidt, L., Grah, A., Klatte, J., Jenson, R., Blackmore, W., Weislogel, M., Dreyer, M.: The capillary channel flow experiments on the international space station: experiment set-up and first results. Exp. Fluids **54**(5), 1519 (2013)

Canfield, P., Zaussinger, F., Egbers, C., Heintzmann, P.: AtmoFlow - simulating atmospheric flows on the international space station. Part I: experiment and ISS-implementation concept. In: 69Th IAC Conference Proceedings, International Astronautical Federation, Vol 18.A2.6.15-69 (2018)

Castellanos, A.: Electrohydrodynamics, vol CISM courses and lectures-380. Springer-Verlag, Wien GmbH (1998)

Chan, S.C., Nigam, S.: Residual diagnosis of diabatic heating from era-40 and ncep reanalyses: Intercomparisons with trmm. J. Climate **22**(2), 414–428 (2009). https://doi.org/10.1175/2008JCLI2417.1

Christensen, U.R.: Zonal flow driven by deep convection in the major planets. Geophys. Res. Lett. **28**(13), 2553–2556 (2001). https://doi.org/10.1029/2000GL012643

Conrath, M., Canfield, P., Bronowicki, P., Dreyer, M.E., Weislogel, M.M., Grah, A.: Capillary channel flow experiments aboard the international space station. Phys. Rev. E **88**(6), 063,009 (2013)

Dietrich, W., Gastine, T., Wicht, J.: Reversal and amplification of zonal flows by boundary enforced thermal wind. Icarus **282**, 380–392 (2017). https://doi.org/10.1016/j.icarus.2016.09.013. http://www.sciencedirect.com/science/article/pii/S0019103516305759

Dubois, F., Joannes, L., Dupont, O., Dewandel, J.L., Legros, J.C.: An integrated optical set-up for fluid-physics experiments under microgravity conditions. Meas. Sci. Technol. **10**(10), 934 (1999). http://stacks.iop.org/0957-0233/10/i=10/a=314

Egbers, C., Brasch, W., Sitte, B., Immohr, J., Schmidt, J.R.: Estimates on diagnostic methods for investigations of thermal convection between spherical shells in space. Meas. Sci. Technol. **10**(10), 866–877 (1999). https://doi.org/10.1088/0957-0233/10/10/306

Egbers, C., Beyer, W., Bonhage, A., Hollerbach, R., Beltrame, P.: The GeoFlow-experiment on ISS (part I): Experimental preparation and design of laboratory testing hardware. Adv. Space Res. **32**(2), 171–180 (2003). https://doi.org/10.1016/S0273-1177(03)90248-1. http://www.sciencedirect.com/science/article/pii/S0273117703902481, gravitational effects in physico-chemical processes

Evgenidis, S.P., Zacharias, K.A., Karapantsios, T.D., Kostoglou, M.: Effect of liquid properties on heat transfer from miniature heaters at different gravity conditions. Microgravity Sci. Technol. **23**(2), 123–128 (2011). https://doi.org/10.1007/s12217-010-9206-9

Ezquerro Navarro, J.M., Fernández, J.J., Rodríguez, J., Laverón-Simavilla, A., Lapuerta, V.: Results and experiences from the execution of the geoflow experiments on the iss. Microgravity Sci. Technol. **27**(1), 61–74 (2015). https://doi.org/10.1007/s12217-015-9413-5

Feudel, F., Tuckerman, L., Gellert, M., Seehafer, N.: Bifurcations of rotating waves in rotating spherical shell convection. Phys. Rev. E **92**(053015) (2015)

Früh, W.G.: Turbbase. https://turbase.cineca.it/init/routes/#/logging/view_dataset/14/tabfile (2018)

Futterer, B., Gellert, M., von Larcher, T., Egbers, C.: Thermal convection in rotating spherical shells: an experimental and numerical approach within GeoFlow. Acta Astronautica **62**(4–5), 300–307 (2008). https://doi.org/10.1016/j.actaastro.2007.11.006. http://www.sciencedirect.com/science/article/pii/S0094576507003013

Futterer, B., Krebs, A., Plesa, A.C., Zaussinger, F., Hollerbach, R., Breuer, D., Egbers, C.: Sheet-like and plume-like thermal flow in a spherical convection experiment performed under microgravity. J. Fluid Mech. **735**, 647–683 (2013). https://doi.org/10.1017/jfm.2013.507. https://www.cambridge.org/core/article/div-class-title-sheet-like-and-plume-like-thermal-flow-in-a-spherical-convection-experiment-performed-under-microgravity-div/32CFFF7061E5F96C8153453826DCFF55

Futterer, B., Dahley, N., Egbers, C.: Thermal electro-hydrodynamic heat transfer augmentation in vertical annuli by the use of dielectrophoretic forces through a.c. electric field. Int. J. Heat Mass Transf. **93**, 144–154 (2016). https://doi.org/10.1016/j.ijheatmasstransfer.2015.10.005. http://www.sciencedirect.com/science/article/pii/S0017931015010030

Gastine, T., Wicht, J., Aurnou, J.: Zonal flow regimes in rotating anelastic spherical shells: an application to giant planets. Icarus **225**(1), 156–172 (2013a). https://doi.org/10.1016/j.icarus.2013.02.031. http://www.sciencedirect.com/science/article/pii/S001910351300119X

Gastine, T., Yadav, R.K., Morin, J., Reiners, A., Wicht, J.: From solar-like to antisolar differential rotation in cool stars. Mon. Not. R. Astron. Soc. Lett. **438**(1), L76–L80 (2013b). https://doi.org/10.1093/mnrasl/slt162

Hart, J.E., Glatzmaier, G.A., Toomre, J.: Space-laboratory and numerical simulations of thermal convection in a rotating hemispherical shell with radial gravity. J. Fluid Mech. **173**, 519–544 (1986). https://doi.org/10.1017/S0022112086001258. https://www.cambridge.org/core/article/div-class-title-space-laboratory-and-numerical-simulations-of-thermal-convection-in-a-rotating-hemispherical-shell-with-radial-gravity-div/E5DC65212D6332D9720933F64AC208D4

Heimpel, M., Aurnou, J., Wicht, J.: Simulation of equatorial and high-latitude jets on jupiter in a deep convection model. Nature **438**(7065), 193–196 (2005). https://doi.org/10.1038/nature04208

Hollerbach, R., Wiener, R.J., Sullivan, I.S., Donnelly, R.J., Barenghi, C.F.: The flow around a torsionally oscillating sphere. Phys. Fluids **14**(12), 4192–4205 (2002). https://doi.org/10.1063/1.1518029

Jehring, L., Egbers, C., Beltrame, P., Chossat, P., Feudel, F., Hollerbach, R., Mutabazi, I., Tuckerman, L.: Geoflow: First results from geophysical motivated experiments inside the fluid science laboratory of columbus. American Institute of Aeronautics and Astronautics, pp 1–15. AIAA 2009-960. https://doi.org/10.2514/6.2009-960 (2009)

Jenson, R.M., Wollman, A.P., Weislogel, M.M., Sharp, L., Green, R., Canfield, P.J., Klatte, J., Dreyer, M.E.: Passive phase separation of microgravity bubbly flows using conduit geometry. Int. J. Multiphase Flow **65**, 68–81 (2014)

Jules, K., McPherson, K., Hrovat, K., Kelly, E.: Initial characterization of the microgravity environment of the international space station: increments 2 through 4. Acta Astronaut. **55**(10), 855–887 (2004). https://doi.org/10.1016/j.actaastro.2004.04.008. http://www.sciencedirect.com/science/article/pii/S0094576504002061

Julien, K., Rubio, A.M., Grooms, I., Knobloch, E.: Statistical and physical balances in low rossby number Rayleigh–Bénard convection. Geophys. Astrophys. Fluid Dyn. **106**(4-5), 392–428 (2012). https://doi.org/10.1080/03091929.2012.696109

Kelley, D.H., Triana, S.A., Zimmerman, D.S., Lathrop, D.P.: Selection of inertial modes in spherical couette flow. Phys. Rev. E Stat. Nonlin. Soft. Matter. Phys. **81**(2 Pt 2), 026,311 (2010). https://doi.org/10.1103/PhysRevE.81.026311

Kuhl, R., Roth, M., Binnenbruck, H., Dreier, W., Forke, R., Preu, P.: The role of sounding rocket microgravity experiments within the german physical sciences programme. In: Warmbein, B. (ed.) 17Th ESA Symposium on European Rocket and Balloon Programmes and Related Research, vol. 590, pp. 503-508. ESA Special Publication (2005)

Liu, M., Egbers, C., Delgado, A., Rath, H.: Investigation of density driven large-scale ocean motion under microgravity. In: Rath, H.J. (ed.), p. 573?581. Springer, Berlin (1992)

Lotto, M.A., Johnson, K.M., Nie, C.W., Klaus, D.M.: The impact of reduced gravity on free convective heat transfer from a finite, flat, vertical plate. Microgravity Sci. Technol. **29**(5), 371–379 (2017). https://doi.org/10.1007/s12217-017-9555-8

Maeder, A.: On the Richardson criterion for shear instabilities in rotating stars. Astron. Astrophys. **299**, 84 (1995)

Mamun, C.K., Tuckerman, L.S.: Asymmetry and hopf bifurcation in spherical couette flow. Phys. Fluids **7**(1), 80–91 (1995). https://doi.org/10.1063/1.868730

Manneville, J.B., Olson, P.: Banded convection in rotating fluid spheres and the circulation of the Jovian atmosphere. Icarus **122**(2), 242–250 (1996). https://doi.org/10.1006/icar.1996.0123. http://www.sciencedirect.com/science/article/pii/S0019103596901232

Meier, M., Jongmanns, M., Meyer, A., Seelig, T., Egbers, C., Mutabazi, I.: Flow pattern and heat transfer in a cylindrical annulus under 1 g and low-g conditions: Experiments. Microgravity Sci. Technol. **30**(5), 699–712 (2018). https://doi.org/10.1007/s12217-018-9649-y

Meyer, A., Jongmanns, M., Meier, M., Egbers, C., Mutabazi, I.: Thermal convection in a cylindrical annulus under a combined effect of the radial and vertical gravity. Comptes Rendus Mécanique **345**(1), 11–20 (2017). https://doi.org/10.1016/j.crme.2016.10.003. http://www.sciencedirect.com/science/article/pii/S1631072116301000, basic and applied researches in microgravity – A tribute to Bernard Zappoli's contribution

Meyer, A., Crumeyrolle, O., Mutabazi, I., Meier, M., Jongmanns, M., Renoult, M.C., Seelig, T., Egbers, C.: Flow patterns and heat transfer in a cylindrical annulus under 1g and low-g conditions: Theory and simulation. Microgravity Sci. Technol. **30**(5), 653–662 (2018). https://doi.org/10.1007/s12217-018-9636-3

Mutabazi, I., Yoshikawa, H.N., Fogaing, M.T., Travnikov, V., Crumeyrolle, O., Futterer, B., Egbers, C.: Thermo-electro-hydrodynamic convection under microgravity: a review. Fluid Dyn. Res. **48**(6), 061,413 (2016). http://stacks.iop.org/1873-7005/48/i=6/a=061413

Platten, J., Legros, J.: Convection in Liquids. Springer, Berlin (2012). https://books.google.de/books?id=S8buCAAAQBAJ

Prodi, F., Santachiara, G., Travaini, S., Vedernikov, A., Dubois, F., Minetti, C., Legros, J.: Measurements of phoretic velocities of aerosol particles in microgravity conditions. Atmospheric Research **82**(1), 183–189 (2006). https://doi.org/10.1016/j.atmosres.2005.09.010. http://www.sciencedirect.com/science/article/pii/S0169809506000342, 14th International Conference on Clouds and Precipitation

Read, P.L., Yamazaki, Y.H., Lewis, S.R., Williams, P.D., Miki-Yamazaki, K., Sommeria, J., Didelle, H., Fincham, A.: Jupiter's and saturn's convectively driven banded jets in the laboratory. Geophys. Res. Lett. 31(22). https://doi.org/10.1029/2004GL020106 (2004)

Renka, R.J.: Algorithm 660: Qshep2d: Quadratic shepard method for bivariate interpolation of scattered data. ACM Trans. Math. Softw. **14**(2), 149–150 (1988). https://doi.org/10.1145/45054.356231. http://doi.acm.org/10.1145/45054.356231

Rice, J.E., Fox, J.C., Lange, W.G., Dietrich, R.W., Wagar, W.O.: Microgravity acceleration measurement system for the international space station (1999)

Rieutord, M., Triana, S.A., Zimmerman, D.S., Lathrop, D.P.: Excitation of inertial modes in an experimental spherical couette flow. Phys. Rev. E Stat. Nonlin. Soft. Matter. Phys. **86**(2 Pt 2), 026,304 (2012). https://doi.org/10.1103/PhysRevE.86.026304

Scolan, H., Read, P.L.: A rotating annulus driven by localized convective forcing: a new atmosphere-like experiment. Exp. Fluids 58 (6). https://doi.org/10.1007/s00348-017-2347-5 (2017)

Shevtsova, V.M., Melnikov, D.E., Legros, J.C.: The study of weak oscillatory flows in space experiments. Microgravity Sci. Technol. **15**(1), 49–61 (2004). https://doi.org/10.1007/BF02870952

Smirnov, N.N., Nikitin, V.F., Ivashnyov, O.E., Maximenko, A., Thiercelin, M., Vedernikov, A., Scheid, B., Legros, J.C.: Microgravity investigations of instability and mixing flux in frontal displacement of fluids. Microgravity Sci. Technol. **15**(2), 35–51 (2004). https://doi.org/10.1007/BF02870957

Travnikov, V., Egbers, C., Hollerbach, R.: The Geoflow-experiment on ISS (Part II): Numerical simulation. Adv. Space Res. **32**(2), 181–189 (2003). https://doi.org/10.1016/S0273-1177(03)90249-3. http://www.sciencedirect.com/science/article/pii/S0273117703902493, gravitational Effects in Physico-Chemical Processes

Travnikov, V., Zaussinger, F., Beltrame, P., Egbers, C.: Influence of the temperature-dependent viscosity on convective flow in the radial force field. Phys. Rev. E. **96**(2) (2017)

Vilella, K., Deschamps, F.: Temperature and heat flux scaling laws for isoviscous, infinite Prandtl number mixed heating convection. Geophys. J. Int. **214**(1), 265–281 (2018). https://doi.org/10.1093/gji/ggy138

Vincze, M., Borchert, S., Achatz, U., von Larcher, T., Baumann, M., Liersch, C., Remmler, S., Beck, T., Alexandrov, K.D., Egbers, C., Fröhlich, J., Heuveline, V., Hickel, S., Harlander, U.: Benchmarking in a rotating annulus: a comparative experimental and numerical study of baroclinic wave dynamics. Meteorologische Zeitschrift **23**(6), 611–635 (2015). https://doi.org/10.1127/metz/2014/0600

Vorontsov, S.V., Christensen-Dalsgaard, J., Schou, J., Strakhov, V.N., Thompson, M.J.: Helioseismic measurement of solar torsional oscillations. Science **296**(5565), 101–103 (2002). https://doi.org/10.1126/science.1069190. https://science.sciencemag.org/content/296/5565/101

Wang, Y., Read, P.: Diversity of planetary atmospheric circulations and climates in a simplified general circulation model. Proceedings IAU Symposium **8**(S293), 297–302 (2012). https://doi.org/10.1017/S1743921313013033. https://www.cambridge.org/core/article/diversity-of-planetary-atmospheric-circulations-and-climates-in-a-simplified-general-circulation-model/F06958904E99B92B8B9B208A3E630E0B

Waszek, L., Irving, J., Deuss, A.: Reconciling the hemispherical structure of earth's inner core with its super-rotation. Nat. Geosci. **4**, 264 EP– (2011). https://doi.org/10.1038/ngeo1083

Weller, H.G., Tabor, G., Jasak, H., Fureby, C.: A tensorial approach to computational continuum mechanics using object-oriented techniques. Comput. Phys. **12**, 620–631 (1998). https://doi.org/10.1063/1.168744

Zaussinger, F., Krebs, A., Travnikov, V., Egbers, C.: Recognition and tracking of convective flow patterns using Wollaston shearing interferometry. Adv. Space Res. **60**(6), 1327–1344 (2017). https://doi.org/10.1016/j.asr.2017.06.028. http://www.sciencedirect.com/science/article/pii/S0273117717304544

Zaussinger, F., Canfield, P., Driebe, T., Egbers, C., Heintzmann, P., Travnikov, V., Froitzheim, A., Haun, P., Meier, M.: Atmoflow - simulating atmospheric flows on the international space station. Part II: experiments and numerical simulations. In: 69th IAC Conference Proceedings, International Astronautical Federation, vol 18.A2.7.18-69 (2018a)

Zaussinger, F., Haun, P., Neben, M., Seelig, T., Travnikov, V., Egbers, C., Yoshikawa, H., Mutabazi, I.: Dielectrically driven convection in spherical gap geometry. Phys. Rev. Fluids **3**, 093,501 (2018b). https://doi.org/10.1103/PhysRevFluids.3.093501. https://link.aps.org/doi/10.1103/PhysRevFluids.3.093501